ADVANCED MATERIALS INTERFACES
www.advmatinterfaces.de

Check for updates

Esaki Diode Behavior in Highly Uniform MoS_2/Silicon Carbide Heterojunctions

Filippo Giannazzo, Salvatore E. Panasci, Emanuela Schilirò, Fabrizio Roccaforte, Antal Koos, Miklos Nemeth, and Béla Pécz*

The heterogeneous integration with 2D materials enables new functionalities and novel devices in state-of-the-art bulk (3D) semiconductors. In this work, highly uniform MoS_2 heterostructures with silicon carbide (4H-SiC) are obtained by a facile synthesis method, highly compatible with semiconductor fab processing, i.e., the sulfurization of predeposited very-thin (≈1.2 nm) Mo films at a temperature of 700 °C. Current–voltage characteristics of MoS_2/n^+-4H-SiC junctions collected by conductive atomic force microscopy show a pronounced negative differential resistance even at room temperature, which is a typical manifestation of band-to-band tunneling between degenerately p^+-/n^+-doped semiconductors. Here, the degenerate p^+-type doping of MoS_2, with $N_{holes} \approx 4 \times 10^{19}$ cm^{-3} evaluated by Raman mapping, is ascribed to the significant MoO_3 content in the film, as demonstrated by X-ray photoelectron spectroscopy analyses. Furthermore, atomic resolution transmission electron microscopy analyses reveal the presence of an ultrathin (≈1 nm) SiO_2 tunneling barrier between MoS_2 and 4H-SiC, formed during the sulfurization process. The observation of Esaki diode behavior in MoS_2 heterojunctions with 4H-SiC opens new perspectives for this material system as a platform for ultrafast low-power consumption digital applications.

1. Introduction

In the last years, the heterogeneous integration of 2D materials with bulk (3D) semiconductors[1] has been explored to enhance the performances of electronic/optoelectronic devices and sensors, and to add them new functionalities. Furthermore, novel/advanced device concepts exploiting vertical current transport through 2D/3D van der Waals (vdW) heterostructures have been demonstrated,[2–5] including graphene hot electron transistors[6–9] for ultrahigh frequency (THz) electronics and MoS_2-based tunnel (Esaki) diodes for ultrafast low-power consumption digital applications.[10,11] Beside silicon, other semiconductors (including group III Nitrides and silicon carbide) have been considered as platform for graphene and 2D materials integration.[8,9,12–14] In this context, silicon carbide represents a very interesting case. Owing to its outstanding physical properties (wide bandgap, high-critical electric field, and thermal conductivity)[15] and high technological maturity, the 4H-SiC polytype is nowadays the material of choice for high-power devices, which are crucial in strategic fields (energy conversion systems, electric vehicles, and trains, ..) for modern economy and society.[16] Recently, silicon carbide is also attracting increasing interest for the fabrication of complementary metal oxide semiconductor circuits able to operate at high temperatures and in harsh or radiation environments,[17] where conventional Si devices fail. The hexagonal SiC polytypes (6H- and 4H-SiC) naturally support the epitaxial growth of 2D materials with hexagonal lattice, including graphene and transition metal dichalcogenides (TMDs). In fact, the epitaxial growth of graphene by high-temperature decomposition of SiC surface[18] or by chemical vapor deposition (CVD) with hydrocarbon gases[19] has been investigated since a long time, and the high-quality epitaxial graphene (EG) enabled the implementation of advanced functionalities (high frequency,[20] sensing,[21] and quantum metrology devices[22]) on the SiC substrate, as well as the fabrication monolithic EG/SiC metal semiconductor field effect transistor devices.[23] In the last years, significant progresses have been achieved in the growth of TMDs by scalable techniques, such as CVD.[24] In particular, the epitaxial growth of semiconducting 2H-MoS_2 on 4H-SiC[25–29] has been recently explored for applications in heterojunction diodes,[25] UV photodetectors,[26] and hydrogen evolution reactions.[29] More specifically, unintentionally doped multilayers of MoS_2 on 4H-SiC have been obtained by one-step CVD at a temperature of 750 °C with vapors from sulfur and MoO_3

F. Giannazzo, S. E. Panasci, E. Schilirò, F. Roccaforte
CNR-IMM
Strada VIII
Catania 5 95121, Italy
E-mail: filippo.giannazzo@imm.cnr.it

S. E. Panasci
Department of Physics and Astronomy
University of Catania
Via Santa Sofia 64, Catania 95123, Italy

A. Koos, M. Nemeth, B. Pécz
Centre for Energy Research
Institute of Technical Physics and Materials Science
Konkoly-Thege ut 29–33, Budapest 1121, Hungary

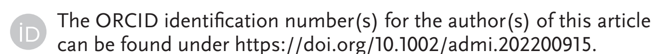
The ORCID identification number(s) for the author(s) of this article can be found under https://doi.org/10.1002/admi.202200915.

© 2022 The Authors. Advanced Materials Interfaces published by Wiley-VCH GmbH. This is an open access article under the terms of the Creative Commons Attribution License, which permits use, distribution and reproduction in any medium, provided the original work is properly cited.

DOI: 10.1002/admi.202200915

powders.[26] The direct growth of p$^+$-doped MoS_2 multilayers on n$^+$ 4H-SiC substrates has been achieved by sulfurization of thin Mo/Nb/Mo stacks at high temperature (1000 °C), where Nb atoms had the role of acceptors for MoS_2.[25] However, the current injection across these p$^+$ MoS_2/n$^+$ SiC heterojunctions was found to be dominated by multistep recombination tunneling through midgap states in SiC, probably associated to interface defects.[25] The band-to-band tunneling (Esaki diode behavior), which typically manifests with negative differential resistance (NDR) in the heterojunction diodes formed by degenerately p$^+$- and n$^+$-doped semiconductors,[30–32] has not been reported so far for p$^+$ MoS_2/n$^+$ SiC heterojunctions, probably due to an insufficient quality of the interface.

As a matter of fact, achieving uniform and high-quality MoS_2/4H-SiC heterojunctions on large area is a key requirement for advanced electronic applications exploiting vertical current injection at the interface.

In our work, highly uniform and controlled coverage of 4H-SiC with ultrathin MoS_2 films (predominantly monolayer (1L)) was achieved by a facile synthesis method,[33] highly compatible with semiconductor fab processes, i.e., sulfurization of predeposited very-thin (≈1.2 nm) Mo films at a temperature of 700 °C. Interestingly, current–voltage characteristics (at room temperature) of these MoS_2 heterojunctions with n$^+$-doped 4H-SiC showed a pronounced NDR, indicating the occurrence of band-to-band-tunneling (BTBT) at the interface. Atomic resolution structural and chemical analyses by scanning transmission electron microscopy (STEM) revealed the presence of an ultrathin (≈1 nm) SiO_2 tunneling barrier between MoS_2 and 4H-SiC, formed during the sulfurization process. The degenerate p$^+$-type doping of MoS_2 (holes concentration $N_h \approx 4 \times 10^{19}$ cm^{-3}) produced by the sulfurization approach, evaluated by Raman spectroscopy, was ascribed to the significant MoO_3 content in the film, demonstrated by X-ray photoelectron spectroscopy (XPS) analyses.

2. Results and Discussion

MoS_2 has been grown on the surface of highly n$^+$-doped (≈10^{19} cm^{-3}) 4H-SiC(0001) 4°-off substrates and of n-doped (≈10^{16} cm^{-3}) 4H-SiC epilayers by sulfurization of predeposited ultrathin Mo films. The as-deposited Mo films (with ≈1.2 nm thickness evaluated by atomic force microscopy (AFM) step height measurements) were found to be completely oxidized, probably due to air exposure. As schematically illustrated in **Figure 1**, the sulfurization process was carried out in quartz tube with two-heating zones. The samples placed in the second zone (at a temperature T_2 = 700 °C) were exposed to sulfur vapors transported by the carrier gas (Ar) from the crucible in the first zone (at T_1 = 150 °C).

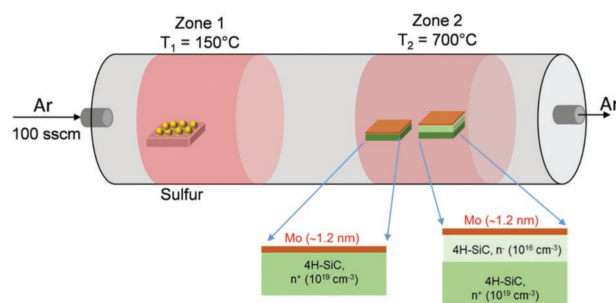

Figure 1. Schematic illustration of MoS_2 growth on n$^+$ 4H-SiC substrate and n$^-$ 4H-SiC epitaxy by sulfurization of a predeposited Mo film.

Figure 2 shows the results of XPS analyses performed both on the as-deposited Mo on 4H-SiC (a,b) and after the sulfurization process (c,d). Mo 3d core level spectra in Figure 2a indicate that the as-deposited ultrathin Mo film was fully oxidized (being MoO_3 the main component, with a minor MoO_2 contribution). After the sulfurization process, the expected Mo3d, S2s, and S2p contributions associated to MoS_2 can be observed in Figure 2c,d, accompanied by minor contributions associated to unreacted MoO_3. As it will be discussed later on in this paper, this MoO_3 component can play a crucial role in the electrical behavior of the MoS_2/4H-SiC heterostructure.

The main mechanism ruling the formation of MoS_2 during the sulfurization process is the heterogeneous vapor–solid reaction between S and MoO_x, while the loss of MoO_x by evaporation plays a not negligible role at the temperature of 700 °C.[34] According to other recent reports,[33,34] the sulfurization of ≈1 nm MoO_x is expected to result in the formation of 1L MoS_2. No reaction between Mo or S and 4H-SiC occurs during the sulfurization process, while a slight oxidation of 4H-SiC is observed, as indicated by Si 2p core level spectra of the as-deposited and annealed samples (reported in Figure S1, Supporting Information).

Figure 3a,b shows the surface morphology of the pristine 4H-SiC n$^+$ substrate and after MoS_2 formation. The conformal coverage of the SiC surface by a nanocrystalline film, with average grain size of ≈50 nm, can be deduced from Figure 3b. The morphology of the bare n$^-$ 4H-SiC epitaxial layer exhibits the typical step bunching associated to the 4°-off miscut angle (Figure 3c), and the coverage by the nanocrystalline MoS_2 film can be argued after the Mo thin film sulfurization (Figure 3d).

The MoS_2 thickness uniformity on the n$^+$ and n$^-$ 4H-SiC was quantitatively evaluated by the Raman mapping. A typical Raman spectrum collected with a laser source of 532 nm on the MoS_2/n$^+$-SiC sample is reported in **Figure 4**a, where the main vibrational features of the 4H-SiC substrate (i.e., E_2(TA), A_2(LA), E_2(TO), E_1(TO), A_1(LO)) and of 2H-MoS_2 (E_{2g} and A_{1g}) have been highlighted. Figure 4b shows a closer view of the in-plane (E_{2g}) and out-of-plane (A_{1g}) vibrational modes of MoS_2, with the indication of the peaks wavenumber difference $\Delta\omega \approx 20.1$ cm^{-1}, which is consistent with monolayer (1L) MoS_2 thickness.[35] Figure 4c,d displays a color map and the histogram of the $\Delta\omega$ values extracted from an array of 50 × 50 Raman spectra collected on 10 µm × 10 µm sample area. From this statistical analysis, an average $\Delta\omega \approx 20.8$ cm^{-1} with a standard deviation of 0.8 cm^{-1} has been deduced, indicating that the film produced by sulfurization is predominantly formed by 1L-MoS_2, with a small fraction of 2L or 3L areas. The same kind of analysis (reported in Figure 4e–h) was carried out on the MoS_2/n$^-$-SiC sample, showing a very similar distribution of MoS_2 number of layers (average $\Delta\omega \approx 20.8$ cm^{-1} with a standard deviation of 0.5 cm^{-1}), in spite of the differences in the surface morphology between the n$^+$-SiC substrate and the epitaxy observed in Figure 3.

After assessing the morphological properties and the thickness uniformity of the as-grown MoS_2 films, the current transport across their heterojunctions with the n$^+$ 4H-SiC and

© 2022 The Authors. Advanced Materials Interfaces published by Wiley-VCH GmbH

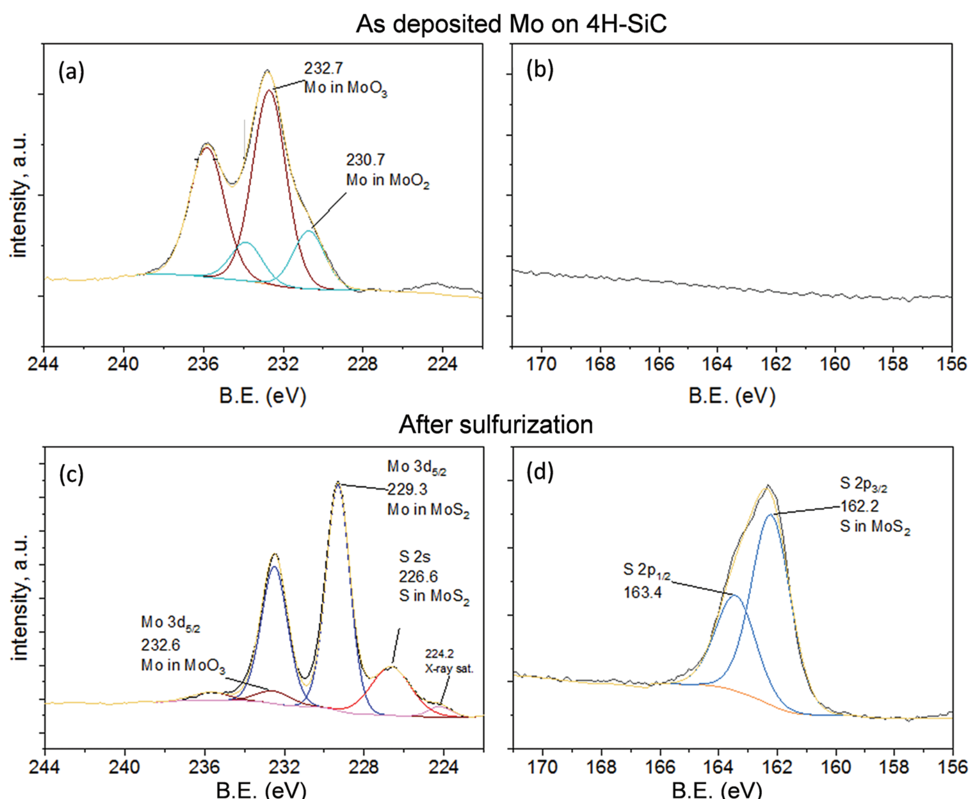

Figure 2. Core level XPS spectra of as-deposited Mo on: a,b) 4H-SiC and c,d) after the sulfurization process.

n^- 4H-SiC has been investigated using conductive atomic force microscopy (C-AFM) with Pt-coated tips, according to the configurations schematically illustrated in **Figure 5**a,d. As compared with conventional current voltage (I–V) measurements on vertical devices with deposited macroscopic electrodes, C-AFM analyses[36] provide spatially resolved information on the injected current with nanoscale resolution, corresponding to the effective contact area of the metal tip. Furthermore, this analysis is nondestructive and allows to probe the intrinsic electrical properties of the MoS_2/4H-SiC heterojunctions, avoiding any effect of contaminations (lithography-induced resist residuals) and modification of the monolayer MoS_2 films by metal deposition during devices fabrication. These metal deposition effects can be particularly relevant, as discussed in recent reference papers.[37,38]

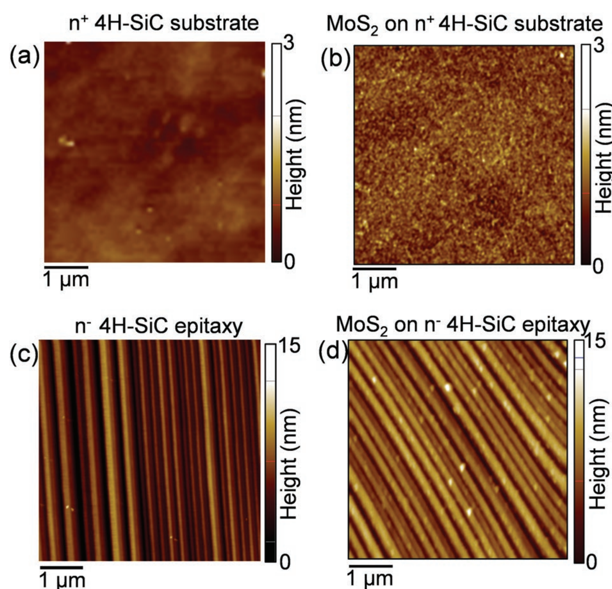

Figure 3. AFM morphologies of the bare surfaces for: a) n^+ 4H-SiC substrate and c) n^- 4H-SiC epitaxy, and b,d) after the MoS_2 growth on the two samples.

Figure 5b shows three I–V characteristics collected by the Pt tip at different positions on the surface of the MoS_2/n^+ SiC heterojunction. The same curves have been reported in a semilog scale in Figure 5c. Similarly, three I–V characteristics at different surface positions of the MoS_2/n^- SiC heterojunction are reported in Figure 5e,f on linear scale and semilog scale, respectively. A noise level in the measured current <50 fA can be observed in the semilog-scale characteristics in Figure 5c,f. The MoS_2 junction with the lightly n-type doped (10^{16} cm^{-3}) 4H-SiC epitaxy exhibits a strongly rectifying behavior, with negligible current injection at negative (reverse) bias and exponential current after a turn on voltage of 4–5 V under positive (forward bias). On the other hand, the I–V characteristics of the MoS_2 heterojunction with the n^+-SiC substrate show much higher current both under reverse and forward bias polarization, as expected by tunneling phenomena across the very narrow depletion region in the degenerately doped 4H-SiC. However, the most noticeable feature in all the curves of Figure 5b,c is the presence of a pronounced negative differential resistance

 © 2022 The Authors. Advanced Materials Interfaces published by Wiley-VCH GmbH

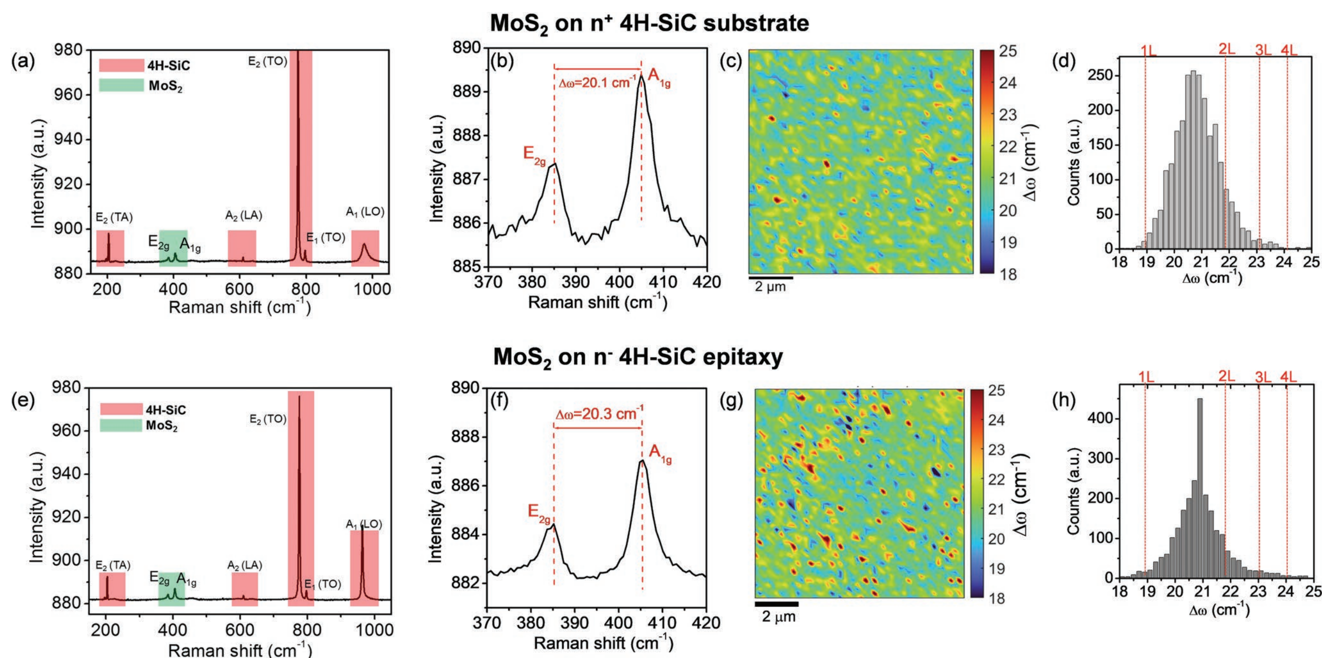

Figure 4. a) Typical Raman spectrum of the MoS_2/n$^+$-SiC sample, with the indication of the main vibrational features of the 4H-SiC substrate and of 2H-MoS_2. b) In-plane (E_{2g}) and out-of-plane (A_{1g}) vibrational modes of MoS_2, with the indication of the peaks wavenumber difference $\Delta\omega \approx 20.1$ cm^{-1}, consistent with monolayer (1L) MoS_2 thickness. c) Color map and d) histogram of the $\Delta\omega$ values extracted from an array of 50 × 50 Raman spectra collected on 10 µm × 10 µm sample area. e) Overview Raman spectrum of the MoS_2/n$^-$-SiC sample and f) detail of MoS_2 vibrational modes. g) Color map and h) histogram of the $\Delta\omega$ values from 50 × 50 Raman spectra collected on 10 µm × 10 µm sample area.

(NDR) under forward polarization, with some variability in the peak voltage (V_P) and peak current (I_P) at the different tip positions. The NDR behavior is typically ascribed to BTBT between degenerately n$^+$- and p$^+$-doped semiconductors. Hence, the observation of this phenomenon in the I–V characteristics of the MoS_2/n$^+$ SiC system at room temperature indicates not only the formation of a very sharp 2D/3D heterojunction but also a degenerate p-type doping of 1L-MoS_2 obtained by the

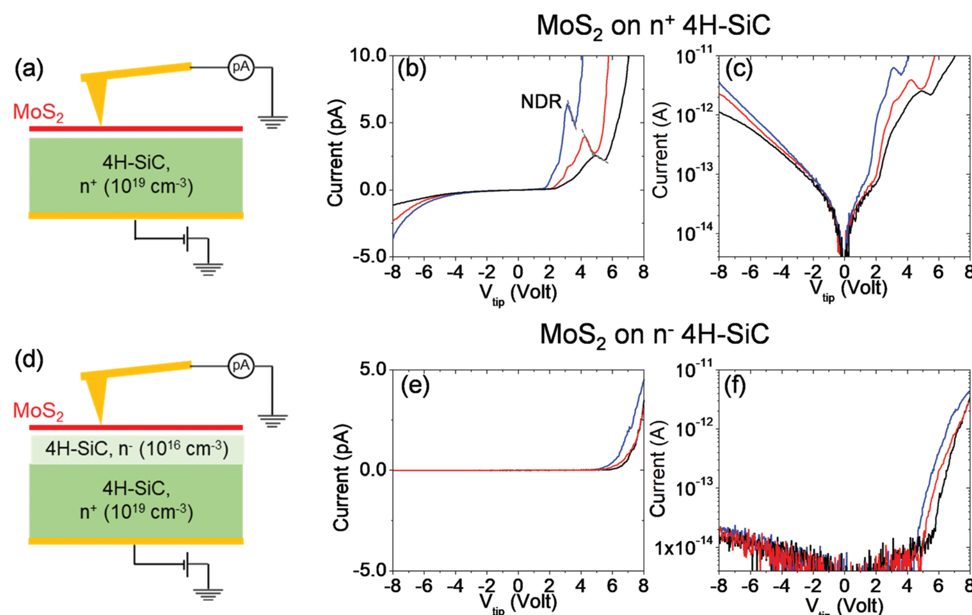

Figure 5. Schematic illustration of the C-AFM setup to probe the current transport through the MoS_2 heterojunctions with the: a) n$^+$ -4H-SiC and d) n$^-$ -4H-SiC. Comparison of three typical I–V characteristics on b) linear and c) semilog-scale, collected by the Pt tip at different positions on the surface of the MoS_2/n$^+$ 4H-SiC heterojunction. Comparison of three typical I–V characteristics on e) linear and f) semilog-scale, at different tip positions on the MoS_2/n$^-$ 4H-SiC heterojunction.

© 2022 The Authors. Advanced Materials Interfaces published by Wiley-VCH GmbH

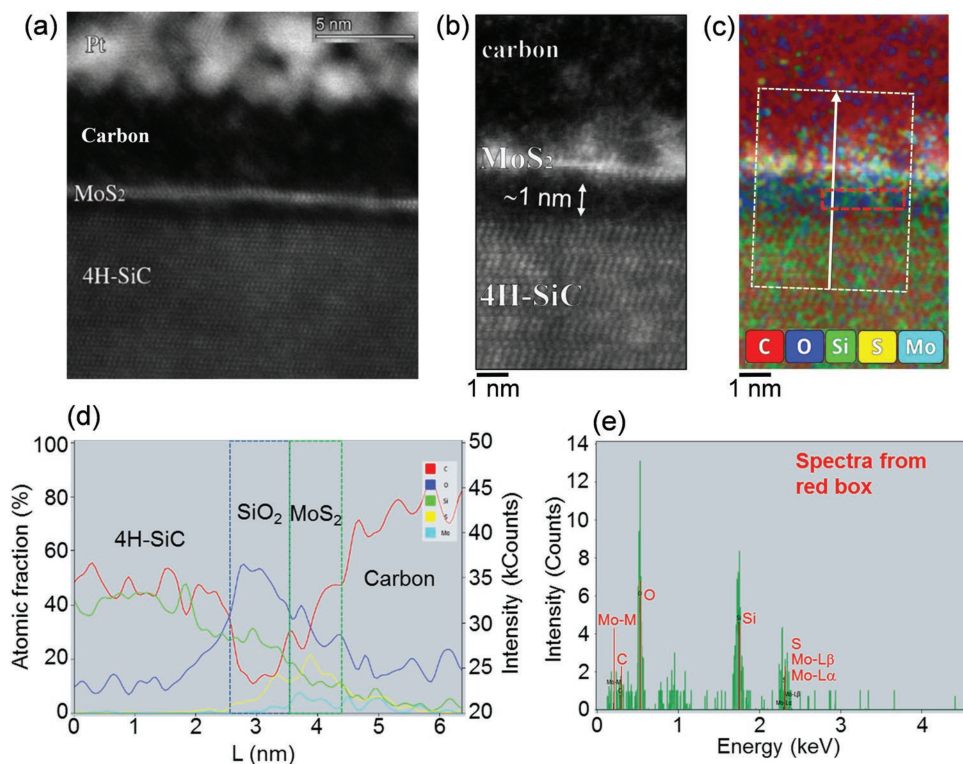

Figure 6. a) HAADF-STEM of the MoS_2 heterojunction with n^+ 4H-SiC. Comparison between b) atomic resolution HAADF and c) EDS elemental map, demonstrating the presence of ≈1 nm SiO_2 at MoS_2/SiC interface. d) Line profile of the atomic fraction versus position extracted from the EDS map. e) X-ray spectra collected from the red-box area c) in the EDS map, from which SiO_2 composition can be deduced.

sulfurization process. The comparison of the three characteristics in Figure 5b,c shows an interesting correlation between the V_P and I_P values under forward bias and the reverse current level, with lower V_P and higher I_P corresponding to a higher reverse current. As discussed in the following, such variability in the local NDR behavior can be ascribed to local changes in the MoS_2 p-type doping.

In the following, atomic resolution electron microscopy investigation of the MoS_2/4H-SiC interface and a detailed analyses of MoS_2 Raman spectra will provide an insight on the origin of the observed Esaki-diode behavior.

Figure 6a shows a low magnification cross-sectional scanning transmission electron microscopy (STEM) image in the high-angle annular dark field (HAADF) mode of the ultrathin MoS_2 film grown on the n^+ 4H-SiC substrate. In this imaging mode, based on Z contrast, MoS_2 appears as a single or double layer with bright contrast. It is covered by a carbon film (with low Z contrast) with a top-most Pt film, used as protective layers during FIB cross-section preparation. Furthermore, a dark stripe is typically present at the interface between MoS_2 and 4H-SiC. Figure 6b shows an atomic resolution HAADF-STEM, from which ≈1 nm thickness of this dark stripe is evaluated.

To get information on the composition of this interfacial region, an EDS spectrum image (Figure 6c) was simultaneously collected, showing the elemental distribution of carbon, oxygen, silicon, molybdenum, and sulfur. Furthermore, a depth profile of atomic fractions extracted from the spectrum image is reported in Figure 6d. On the left, we can see a composition, which belongs to the 4H-SiC substrate. Then, in the middle, where oxygen concentration (blue line) increased, we observe a SiO_2 composition. Then, one can observe the MoS_2 stripe, covered by the protective carbon film. Furthermore, Figure 6e shows an EDS spectrum collected in the rectangular box region in (c), corresponding to the dark stripe in the Z contrast image (b). This compositional analysis clarifies that the ≈1 nm dark stripe between MoS_2 and 4H-SiC observed in the HAADF image (Figure 6b) is SiO_2, formed during the high-temperature sulfurization of the original metal (oxide), as indicated also by XPS analyses (see Figure S1, Supporting Information).

Figure 7a shows a correlative plot of the A_{1g} and E_{2g} Raman peaks' wavenumbers (ω_{A1g} vs ω_{E2g}), obtained from a large array of 2500 spectra measured on MoS_2 on n^+-SiC. This plot provides quantitative information on the doping and strain status of the MoS_2 film, by comparing the distribution of experimental data (open circles) with the theoretical ω_{A1g}–ω_{E2g} relations for a purely strained 1L MoS_2 (strain line) and for a purely doped 1L MoS_2 (doping line).[39]

The strain (doping) lines are represented by the red (black) solid lines in Figure 7a, and their crossing point corresponds to the literature values ω^0_{E2g} = 385 cm^{-1}, ω^0_{A1g} = 405 cm^{-1} (at 532 nm excitation wavelength) for a suspended 1L MoS_2 membrane,[40] which is a good approximation for an ideally unstrained and undoped film. The strain line separates the p-type and n-type doping regions in the ω_{A1g}–ω_{E2g} plot, whereas the doping line separates the tensile and compressive strain regions. Hence, the experimental data distribution in Figure 7a clearly shows that the MoS_2 film produced by Mo sulfurization

 © 2022 The Authors. Advanced Materials Interfaces published by Wiley-VCH GmbH

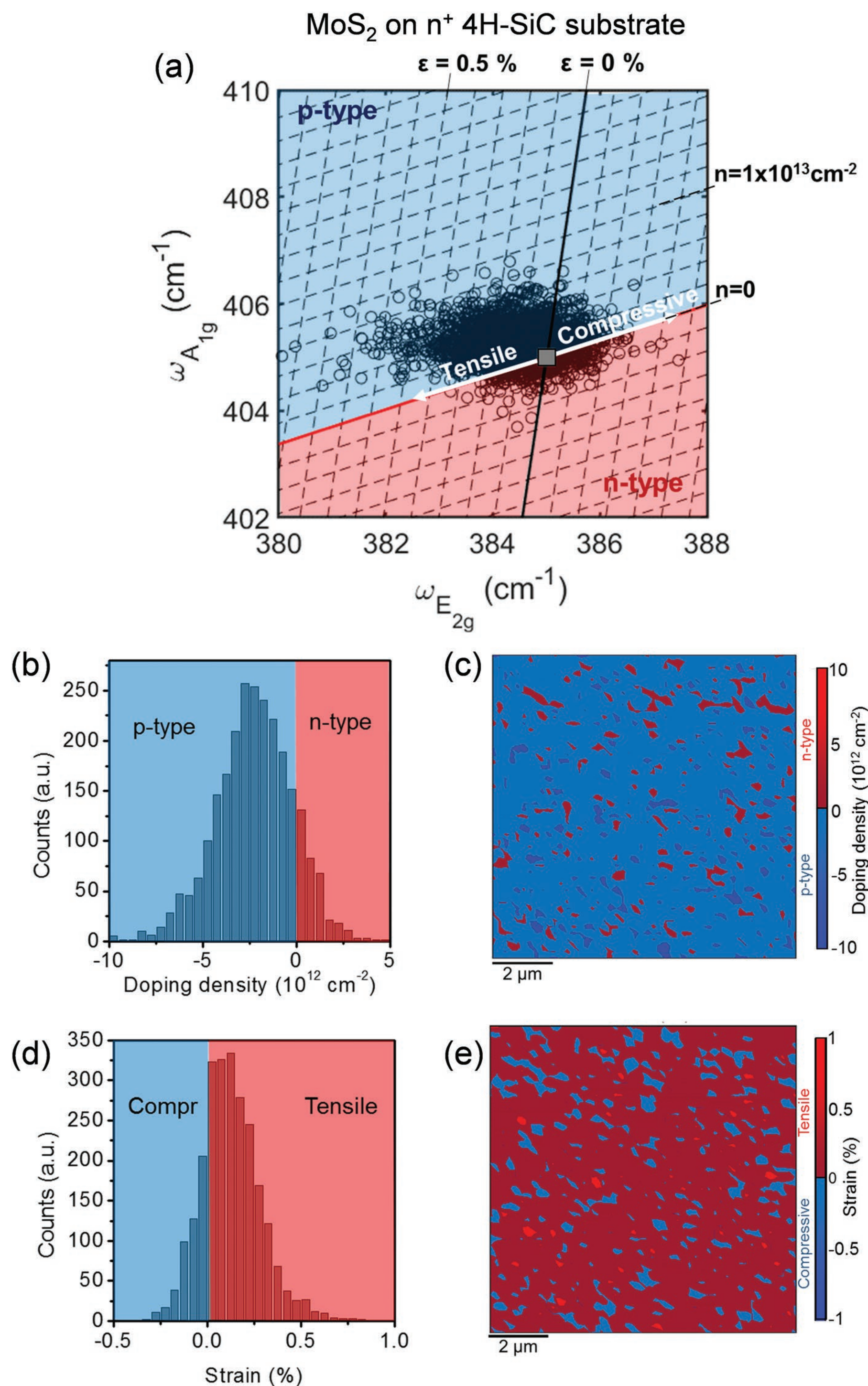

Figure 7. a) Correlative plot of the A_{1g} and E_{2g} Raman peaks' wavenumbers extracted from the array of 50 × 50 Raman spectra on 10 µm × 10 µm sample area in Figure 4. b) Histogram and c) map of the MoS_2 doping density. d) Histogram and e) map of the MoS_2 strain.

exhibits a p-type doping in most of the probed area and exhibits a small tensile strain (<0.5%). Furthermore, the dashed lines parallel to the strain (doping) lines allow to estimate on the doping (strain) values associated at each data point. The histogram and the corresponding map of the doping density values have been reported in Figure 7b,c, respectively. Their combination indicates the occurrence of p-type doping on ≈86.4% of the probed MoS_2 area, with an average hole density of 2.5×10^{12} cm^{-2} and a standard deviation of 2×10^{12} cm^{-2}. Analogously, the occurrence of a small tensile strain on ≈79.8% of the probed area, with an average $\varepsilon = 0.12\%$ and a standard deviation of 0.14%, have been deduced from the histogram and the color

 © 2022 The Authors. Advanced Materials Interfaces published by Wiley-VCH GmbH

map in Figure 7d,e. Furthermore, the comparison of the two maps in Figure 7c,e indicates the lack of correlation between the doping and strain spatial distributions in the MoS_2 film.

The same kind of analysis has been carried out on the array of Raman spectra collected on MoS_2 grown on the n^- 4H-SiC epitaxy, and similar mean values of MoS_2 doping and strain were obtained (see Figure S2, Supporting Information).

In the case of 1L MoS_2 (with a thickness t ≈ 0.65 nm[41]), an average hole density of 2.5×10^{12} cm^{-2} corresponds to an average concentration of $N_h \approx 4 \times 10^{19}$ cm^{-3}. This value is larger than the effective density of states in the valence band $N_v \approx 1.2 \times 10^{19}$ cm^{-3} for 1L MoS_2, estimated by using a parabolic valence-band model and the corresponding analytical formula

$$N_V = 2\left(\frac{2\pi m_h kT}{h^2}\right)^{\frac{3}{2}} \quad (1)$$

where k is the Boltzmann constant, h is the Planck constant, T = 300 K, and $m_h = 0.61\ m_e$ is the holes effective mass for 1L MoS_2.[42] Hence, the assumption of a degenerately p-type-doped MoS_2 is justified by the results of Raman analyses. On the other hand, the histogram in Figure 7b also shows a lateral variation of the hole doping in the MoS_2 layer, which allows to explain the spatial variability of the NDR in the I–V characteristic collected at different surface positions by the C-AFM tip (see Figure 5b,c).

The origin of this p-type doping can be associated to the presence of a significant MoO_3 fraction in the ultrathin MoS_2 film produced by the sulfurization process, as indicated by XPS analysis. In fact, several recent studies reported on the p-type conduction in MoS_2 by unintentional incorporation of oxygen, e.g., during the growth,[43] or by postdeposition oxygen plasma treatments.[44,45] Furthermore, the formation of shallow acceptor levels in oxygen-doped MoS_2 has been indicated by first principle calculations.[45]

In the following, the forward bias I–V characteristics of the p^+-MoS_2/SiO_2/n^+-SiC heterojunction are discussed in detail, considering the different mechanisms ruling current injection at the interfaces. The equivalent circuit of this system, schematically depicted in **Figure 8**a, can be described by the series combination of the contact resistance R_c associated to the tip/MoS_2 Schottky barrier[46] and of the p^+-MoS_2/SiO_2/n^+-SiC tunnel (Esaki) diode. Hence, the applied tip bias $V_{tip} > 0$ partially drops across the contact resistance and partially across the diode. Figure 8b shows a typical forward bias I–V characteristic measured on the heterojunction. At low forward bias values ($V_{tip} < 3$ V), the current injection is limited by the Pt tip/MoS_2 contact resistance. The semilog-scale plot of the I–V curve in this low current regime, reported in insert of Figure 8b, shows that current transport is limited by direct tunneling (DT) across the Pt/MoS_2 Schottky barrier from 0 to 2 V, being $I_{DT} \propto V_{tip}T$ with T the tunnel probability. Field emission (FE) across the barrier becomes the dominant mechanism between 2 and 3 V.

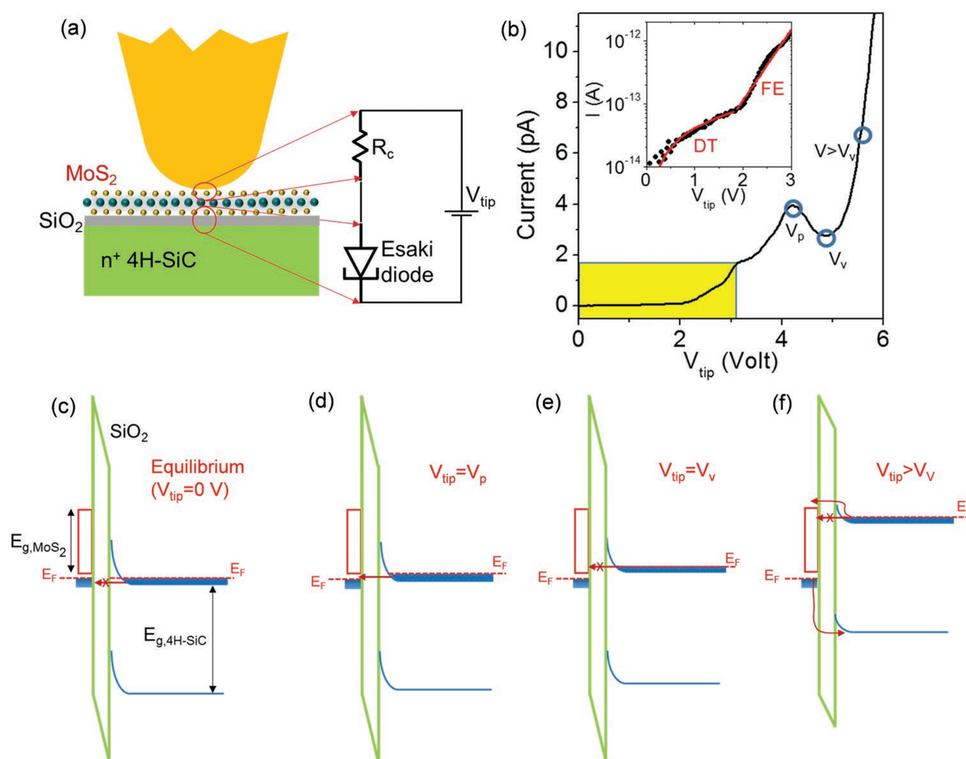

Figure 8. a) Schematic illustration of the Pt tip/MoS_2/SiO_2/SiC junction, with its equivalent circuit, consisting of the series combination of the Pt/MoS_2 contact resistance (R_C) and the Esaki diode. b) Forward bias I–V characteristic with the indication of the different transport regimes. A semilog scale plot of the I–V curve in the low bias regime, dominated by R_C, is reported in the insert. Schematic band diagrams of the p^+-MoS_2/SiO_2/n^+-SiC junction under c) equilibrium conditions, d) at a bias V_p corresponding to the peak current, e) at a bias V_V corresponding to the valley current, and f) for $V_{tip} > V_v$.

© 2022 The Authors. Advanced Materials Interfaces published by Wiley-VCH GmbH

In particular, the FE current increases with the forward bias as $I_{FE} \propto \exp[qV_{tip}/E_{00}]$, being the q the electron charge and E_{00} a characteristic energy related to the holes concentration N_h in the p^+-MoS_2 layer:

$$E_{00} = \frac{h}{\pi}\sqrt{\frac{N_h}{m_h \varepsilon_0 \varepsilon_r}} \tag{2}$$

with ε_0 the vacuum dielectric constant, $\varepsilon_r \approx 6$ the relative permittivity,[47] and m_h the holes effective mass for 1L MoS_2. A value of $E_{00} \approx 377$ meV was obtained from the I–V curve fit in the insert of Figure 8b, from which a hole concentration $N_h \approx 6.9 \times 10^{19}$ cm^{-3} (i.e., a hole density, $n \approx 4.5 \times 10^{12}$ cm^{-2}), in the range of values deduced by Raman mapping.

At forward bias $V_{tip} > 3$ V, the BTBT at the heterojunction becomes the dominant transport mechanism, resulting first in the current increase up to the peak value (I_P) at the voltage V_P, followed by the decrease at the valley current (I_V) at the bias V_v as indicated in Figure 8b. To better illustrate the BTBT phenomenon, the energy band diagrams of the p^+-MoS_2/SiO_2/n^+-SiC system under different biasing conditions are reported in Figure 8c–f. Furthermore, Figure S3 (Supporting Information) shows the alignment between the bands of p^+-doped 1L MoS_2, SiO_2, and n^+ 4H-SiC separated by vacuum, evaluated using the literature values of electron affinity and energy bandgap for these materials.[48–50]

Under equilibrium conditions, i.e., at $V_{tip} = 0$ V (Figure 8c), the Fermi levels of the two degenerate semiconductors are aligned. The thickness of the tunnel barrier between the two semiconductors is the sum of the SiO_2 interfacial layer (≈1 nm) and the depletion region of the n^+-SiC at $V_{tip} = 0$ V, corresponding to the Debye length $L_D = (\varepsilon_0 \varepsilon_{SiC} kT/qN_D)^{1/2} \approx 1.1$ nm for $N_D \approx 10^{19}$ cm^{-3}. Under equilibrium, the filled states of the n^+-SiC conduction band are aligned with the filled states of p^+-MoS_2 valence band and BTBT is forbidden. When high-enough positive bias is applied, filled states on the SiC side, and unoccupied states on the MoS_2 side are partially overlapped, thus the electrons can tunnel through the barrier from n-SiC to p-MoS_2.The BTBT current reaches its maximum (peak current I_p) at the bias $V_{tip} = V_{P,}$ when the overlap between the filled and empty states at the two sides of the barrier reaches its maximum, as illustrated in Figure 8d. By further increasing the V_{tip} the overlap starts to decrease, giving rise to a decrease of the BTBT current, i.e., to the NDR part of the curve. Ideally, the BTBT current is expected to decrease to zero at the bias $V_{tip} = V_{V,}$ when the conduction band edge of SiC and the valence band edge of MoS_2 are aligned (as illustrated in Figure 8e). However, the actual measured value of I_V and, hence, the peak-to-valley current ratio of ≈1.5, can be explained by the occurrence of other competitive transport mechanisms, such as current tunneling mediated by defects states at the interface.[51] For larger bias values ($V_{tip} > V_V$), current transport is ruled by a combined thermionic-tunneling mechanism through the tunnel barrier, as schematically depicted in Figure 8e.

The reported results demonstrate an efficient method to obtain large area and uniform p^+ MoS_2 films on 4H-SiC, which is compatible with semiconductor industry process flows. Furthermore, the observation of room temperature NDR behavior in MoS_2/SiC heterojunctions paves the way to the implementation of Esaki diodes on the silicon carbide platform, extending its range of potential applications to fast switching devices and circuits.

3. Materials and Methods

3.1. Materials Growth

The thin (1.2 nm) Mo films on n^+ 4H-SiC substrates and n^- 4H-SiC epilayer were obtained by DC magnetron sputtering from a Mo-target (using a Quorum Q300-TD system). The sulfurization process was carried out in a two-heating zones furnace, with the first zone (at a temperature of 150 °C) hosting a crucible with 300 mg sulfur, and the second zone (at a temperature of 700 °C) hosting the Mo/SiC samples. Starting from a base pressure of 4×10^{-6} bar, the Ar carrier gas (with a flux of 100 sccm) transported the S vapors from the first to the second zone. The duration of the sulfurization process was 60 min.

3.2. AFM Morphology and Conductive AFM Analyses

Morphological analyses were carried out by Tapping mode Atomic Force Microscopy using a DI3100 system by Bruker with Nanoscope V electronics. Furthermore, nanoscale resolution current-voltage characterization of MoS_2/SiC heterojunctions was performed by Conductive Atomic Force Microscopy (C-AFM) at room temperature and under ambient conditions, using Pt-coated Si tips with ≈5 nm curvature radius.

3.3. XPS Analyses

The compositional properties of the as-deposited metal films and MoS_2 formation after the sulfurization process were evaluated by XPS using an XSAM 800 XPS instrument by Kratos Analytical (Manchester, UK), with a non-monochromatic Mg $K\alpha$ X-ray source (energy = 1253.6 eV). The spectra were collected at a take-off angle of 90° relative to sample surface and pass energy of 40 eV. The instrument resolution is 1.1 eV (Au $4f_{7/2}$, pass energy of 5 eV). The spectra were aligned using the C-Si (silicon carbide) component of C1s (283.1 eV) as reference.

3.4. STEM and EDS Analyses

High-angle annular dark field scanning transmission electron microscopy (HAADF-STEM) and energy dispersion spectroscopy (EDS) analyses of the MoS_2/4H-SiC heterojunctions were carried out with an aberration-corrected Titan Themis 200 microscope. To this aim, cross-sectioned samples were prepared by focused ion beam (FIB), after depositing a carbon/Pt protective layer on MoS_2 surface.

3.5. Raman Analyses

Raman spectroscopy and mapping of MoS_2 vibrational peaks were carried out by a WiTec Alpha equipment, using a laser excitation at 532 nm, 1.5 mW power, and $100 \times$ objective.

© 2022 The Authors. Advanced Materials Interfaces published by Wiley-VCH GmbH

3.6. Statistical Analysis

In this paper, the statistical analysis was performed on the results of Raman mapping reported in Figures 4 and 7. Arrays of 50 × 50 Raman spectra on 10 µm × 10 µm areas were collected both on the MoS_2/n^+ 4H-SiC and MoS_2/n^- 4H-SiC samples. For each array, individual Raman spectra were extracted using the Witec software. A Matlab code written by the authors was used to evaluate the E_{2g} and A_{1g} vibrational peaks wavenumbers (ω_{E2g} and ω_{A1g}) for all the spectra, and to generate the color maps/hystograms of $\Delta\omega$ in Figure 4c,d,g,h. The average value of $\Delta\omega$ and its standard deviation were calculated from these distributions. The Matlab code was also used to build the correlative plot of ω_{E2g}, ω_{A1g} wavenumbers in Figure 7a and to evaluate the maps/hystograms of local strain and doping values on the MoS_2 in Figure 7b–e. The average value of the strain and doping and their standard deviation were calculated from these strain/doping distributions.

Supporting Information

Supporting Information is available from the Wiley Online Library or from the author.

Acknowledgements

S. Di Franco (CNR-IMM, Catania) is acknowledged for the expert technical assistance with samples preparation. G. Greco and P. Fiorenza (CNR-IMM, Catania), S. Agnello, M. Cannas, and F. M. Gelardi (Univ. of Palermo), Y. Cordier, A. Michon, and M. Al Khalfioui (CNRS-CRHEA, France), S. Chromik and M. Spankova (IEE-SAS, Slovakia) are acknowledged for useful discussions. This work was funded, in part, by MUR in the framework of the FlagERA-JTC 2019 project ETMOS. B.P. and A.K. acknowledge funding from the national projects TKP2021-NKTA-05 and NKFIH K_134258. Part of the experiments was carried out using the facilities of the Italian Infrastructure Beyond Nano.

Open access Funding provided by Consiglio Nazionale delle Ricerche within the CRUI-CARE Agreement.

Conflict of Interest

The authors declare no conflict of interest.

Data Availability Statement

The data that support the findings of this study are available from the corresponding author upon reasonable request.

Keywords

2D materials, Esaki diode, MoS_2, silicon carbide

Received: April 24, 2022
Revised: May 24, 2022
Published online:

[1] D. Jariwala, T. J. Marks, M. C. Hersam, *Nat. Mater.* **2017**, *16*, 170.
[2] J. Miao, X. Liu, K. Jo, K. He, R. Saxena, B. Song, H. Zhang, J. He, M.-G. Han, W. Hu, D. Jariwala, *Nano Lett.* **2020**, *20*, 2907.
[3] Z. Wang, A. Hemmetter, B. Uzlu, M. Saeed, A. Hamed, S. Kataria, R. Negra, D. Neumaier, M. C. Lemme, *Adv. Electron. Mater.* **2021**, *7*, 2001210.
[4] F. Giannazzo, G. Greco, F. Roccaforte, S. Sonde, *Crystals* **2018**, *8*, 70.
[5] D. Ruzmetov, K. Zhang, G. Stan, B. Kalanyan, G. R. Bhimanapati, S. M. Eichfeld, R. A. Burke, P. B. Shah, T. P. O'regan, F. J. Crowne, A. G. Birdwell, J. A. Robinson, A. V. Davydov, T. G. Ivanov, *ACS Nano* **2016**, *10*, 3580.
[6] S. Vaziri, G. Lupina, C. Henkel, A. D. Smith, M. Östling, J. Dabrowski, G. Lippert, W. Mehr, M. C. Lemme, *Nano Lett.* **2013**, *13*, 1435.
[7] C. Zeng, E. B. Song, M. Wang, S. Lee, C. M. Torres, J. Tang, B. H. Weiller, K. L. Wang, *Nano Lett.* **2013**, *13*, 2370.
[8] A. Zubair, A. Nourbakhsh, J.-Y. Hong, M. Qi, Y. Song, D. Jena, J. Kong, M. Dresselhaus, T. Palacios, *Nano Lett.* **2017**, *17*, 3089.
[9] F. Giannazzo, G. Greco, E. Schilirò, R. Lo Nigro, I. Deretzis, A. La Magna, F. Roccaforte, F. Iucolano, S. Ravesi, E. Frayssinet, A. Michon, Y. Cordier, *ACS Appl. Electron. Mater.* **2019**, *1*, 2342.
[10] K. Xu, Y. Cai, W. Zhu, *IEEE Trans. Electron Devices* **2018**, *65*, 4155.
[11] S. Krishnamoorthy, E. W. Lee, C. H. Lee, Y. Zhang, W. D. Mcculloch, J. M. Johnson, J. Hwang, Y. Wu, S. Rajan, *Appl. Phys. Lett.* **2016**, *109*, 183505.
[12] G. Fisichella, G. Greco, F. Roccaforte, F. Giannazzo, *Nanoscale* **2014**, *6*, 8671.
[13] H. Jeong, S. Bang, H. M. Oh, H. J. Jeong, S.-J. An, G. H. Han, H. Kim, K. K. Kim, J. C. Park, Y. H. Lee, G. Lerondel, M. S. Jeong, *ACS Nano* **2015**, *9*, 10032.
[14] F. Giannazzo, R. Dagher, E. Schilirò, S. E. Panasci, G. Greco, G. Nicotra, F. Roccaforte, S. Agnello, J. Brault, Y. Cordier, A. Michon, *Nanotechnology* **2020**, *32*, 015705.
[15] T. Kimoto, J. A. Cooper, *Fundamentals of Silicon Carbide Technology*, John Wiley & Sons, Singapore **2014**; p. 20.
[16] F. Roccaforte, P. Fiorenza, G. Greco, R. Lo Nigro, F. Giannazzo, F. Iucolano, M. Saggio, *Microelectron. Eng.* **2018**, *187–188*, 66.
[17] J. Romijn, S. Vollebregt, L. M. Middelburg, B. E.l Mansouri, H. W. Van Zeijl, A. May, T. Erlbacher, G. Zhang, P. M. Sarro, *IEEE Trans. Electron Devices* **2021**, 4, https://doi.org/10.1109/TED.2021.3125279.
[18] K. V. Emtsev, A. Bostwick, K. Horn, J. Jobst, G. L. Kellogg, L. Ley, J. L. Mcchesney, T. Ohta, S. A. Reshanov, J. Röhrl, E. Rotenberg, A. K. Schmid, D. Waldmann, H. B. Weber, T. Seyller, *Nat. Mater.* **2009**, *8*, 203.
[19] W. Strupinski, K. Grodecki, A. Wysmolek, R. Stepniewski, T. Szkopek, P. E. Gaskell, A. Grüneis, D. Haberer, R. Bozek, J. Krupka, J. M. Baranowski, *Nano Lett.* **2011**, *11*, 1786.
[20] Y.-M. Lin, C. Dimitrakopoulos, K. A. Jenkins, D. B. Farmer, H.-Y. Chiu, A. Grill, Ph. Avouris, *Science* **2010**, *327*, 662.
[21] C. Melios, V. Panchal, K. Edmonds, A. Lartsev, R. Yakimova, O. Kazakova, *ACS Sens.* **2018**, *3*, 1666.
[22] A. Tzalenchuk, S. Lara-Avila, A. Kalaboukhov, S. Paolillo, M. Syväjärvi, R. Yakimova, O. Kazakova, T. J. B. M. Janssen, V. Fal'ko, S. Kubatkin, *Nat. Nanotechnol.* **2010**, *5*, 186.
[23] S. Hertel, D. Waldmann, J. Jobst, A. Albert, M. Albrecht, S. Reshanov, A. Schöner, M. Krieger, H. B. Weber, *Nat. Commun.* **2012**, *3*, 957.
[24] K. Hernandez Ruiz, Z. Wang, M. Ciprian, M. Zhu, R. Tu, L. Zhang, W. Luo, Y. Fan, W. Jiang, *Small Sci.* **2022**, *2*, 2100047.
[25] E. W. LeeII, L. Ma, D. N. Nath, C. H. Lee, A. Arehart, Y. Wu, S. Rajan, *Appl. Phys. Lett.* **2014**, *105*, 203504.
[26] Y. Xiao, L. Min, X. Liu, W. Liu, U. Younis, T. Peng, X. Kang, X. Wu, S. Ding, D. W. Zhang, *Nanophotonics* **2020**, *9*, 3035.
[27] D. Wu, T. Min, J. Zhou, C. Li, G. Ma, G. Lu, M. Xia, Z. Gu, *Sci. Rep.* **2017**, *7*, 15166.

© 2022 The Authors. Advanced Materials Interfaces published by Wiley-VCH GmbH

[28] A. M. Dubrovkin, B. Qiang, H. N. S. Krishnamoorthy, N. I. Zheludev, Q. J. Wang, *Nat. Commun.* **2018**, *9*, 1762.
[29] F. Lan, Z. Lai, Y. Xu, H. Cheng, Z. Wang, C. Qi, J. Chen, S. Zhang, *Sci. Rep.* **2016**, *6*, 31980.
[30] L. Esaki, *Phys. Rev.* **1958**, *109*, 603.
[31] A. M. Ionescu, H. Riel, *Nature* **2011**, *479*, 329.
[32] H. Lu, A. Seabaugh, *IEEE J. Electron Devices Soc.* **2014**, *2*, 44.
[33] S. E. Panasci, A. Koos, E. Schilirò, S. Di Franco, G. Greco, P. Fiorenza, F. Roccaforte, S. Agnello, M. Cannas, F. M. Gelardi, A. Sulyok, M. Nemeth, B. Pécz, F. Giannazzo, *Nanomaterials* **2022**, *12*, 182.
[34] S. Vangelista, E. Cinquanta, C. Martella, M. Alia, M. Longo, A. Lamperti, R. Mantovan, F. B. Basset, F. Pezzoli, A. Molle, *Nanotechnology* **2016**, *27*, 175703.
[35] C. Lee, H. Yan, L. E. Brus, T. F. Heinz, J. Hone, S. Ryu, *ACS Nano* **2010**, *4*, 2695.
[36] F. Giannazzo, E. Schilirò, G. Greco, F. Roccaforte, *Nanomaterials* **2020**, *10*, 803.
[37] Y. Liu, J. Guo, E. Zhu, L. Liao, S.-J. Lee, M. Ding, I. Shakir, V. Gambin, Y. Huang, X. Duan, *Nature* **2018**, *557*, 696.
[38] Y. Wang, J. C. Kim, R. J. Wu, J. Martinez, X. Song, J. Yang, F. Zhao, A. Mkhoyan, H. Y. Jeong, M. Chhowalla, *Nature* **2019**, *568*, 70.
[39] S. E. Panasci, E. Schilirò, G. Greco, M. Cannas, F. M. Gelardi, S. Agnello, F. Roccaforte, F. Giannazzo, *ACS Appl. Mater. Interfaces* **2021**, *13*, 31248.
[40] D. Lloyd, X. Liu, J. W. Christopher, L. Cantley, A. Wadehra, B. L. Kim, B. B. Goldberg, A. K. Swan, J. S. Bunch, *Nano Lett.* **2016**, *16*, 5836.
[41] B. Radisavljevic, A. Radenovic, J. Brivio, V. Giacometti, A. Kis, *Nat. Nanotechnol.* **2011**, *6*, 147.
[42] J. Xi, T. Zhao, D. Wang, Z. Shuai, *J. Phys. Chem. Lett.* **2014**, *5*, 285.
[43] A. T. Neal, R. Pachter, S. Mou, *Appl. Phys. Lett.* **2017**, *110*, 193103.
[44] F. Giannazzo, G. Fisichella, G. Greco, S. Di Franco, I. Deretzis, A. La Magna, C. Bongiorno, G. Nicotra, C. Spinella, M. Scopelliti, B. Pignataro, S. Agnello, F. Roccaforte, *ACS Appl. Mater. Interfaces* **2017**, *9*, 23164.
[45] S. Wu, Y. Zeng, X. Zeng, S. Wang, Y. Hu, W. Wang, S. Yin, G. Zhou, W. Jin, T. Ren, Z. Guo, J. Lu, *2D Mater.* **2019**, *6*, 025007.
[46] F. Giannazzo, G. Fisichella, A. Piazza, S. Agnello, F. Roccaforte, *Phys. Rev. B* **2015**, *92*, 081307(R).
[47] A. Laturia, M. L. Van De Put, W. G. Vandenberghe, *NPJ 2D Mater. Appl.* **2018**, *2*, 6.
[48] H. Lee, S. Deshmukh, J. Wen, V. Z. Costa, J. S. Schuder, M. Sanchez, A. S. Ichimura, E. Pop, B. Wang, A. K. M. Newaz, *ACS Appl. Mater. Interfaces* **2019**, *11*, 31543.
[49] R. Williams, *Phys. Rev.* **1965**, *140*, A569.
[50] S. Y. Davydov, *Semiconductors* **2007**, *41*, 696.
[51] S. M. Sze, K. K. Ng, *Physics of Semiconductor Devices*, 3rd ed., John Wiley & Sons, Hoboken, New Jersey **2007**.

© 2022 The Authors. Advanced Materials Interfaces published by Wiley-VCH GmbH